

Article

Rhombohedral $\text{Li}_{1+x}\text{Y}_x\text{Zr}_{2-x}(\text{PO}_4)_3$ Solid Electrolyte Prepared by Hot-Pressing for All-Solid-State Li-Metal Batteries

Qinghui Li ¹, Chang Xu ², Bing Huang ^{2,3,*} and Xin Yin ^{1,*}

¹ College of Electrical and Information Engineering, Hunan University, Changsha 410082, China; B12090021@hnu.edu.cn

² State Key Laboratory of New Ceramics and Fine Processing, School of Materials Science and Engineering, Tsinghua University, Beijing 100084, China; MSeXuchang@outlook.com

³ School of Materials Science and Engineering, Tianjin University, Tianjin 300072, China

* Correspondence: huangbing@tju.edu.cn (B.H.); yinxin@hnu.edu.cn (X.Y.)

Received: 20 February 2020; Accepted: 31 March 2020; Published: 6 April 2020



Abstract: NASICON-type solid electrolytes with excellent stability in moisture are promising in all-solid-state batteries and redox flow batteries. However, NASICON $\text{LiZr}_2(\text{PO}_4)_3$ (LZP), which is more stable with lithium metal than the commercial $\text{Li}_{1.3}\text{Al}_{0.3}\text{Ti}_{1.7}(\text{PO}_4)_3$, exhibits a low Li-ion conductivity of $10^{-6} \text{ S cm}^{-1}$ because the fast conducting rhombohedral phase only exists above 50°C . In this paper, the high-ionic conductive rhombohedral phase is stabilized by Y^{3+} doping at room temperature, and the hot-pressing technique is employed to further improve the density of the pellet. The dense $\text{Li}_{1.1}\text{Y}_{0.1}\text{Zr}_{1.9}(\text{PO}_4)_3$ pellet prepared by hot-pressing shows a high Li-ion conductivity of $9 \times 10^{-5} \text{ S cm}^{-1}$, which is two orders of magnitude higher than that of $\text{LiZr}_2(\text{PO}_4)_3$. The in-situ formed Li_3P layer on the surface of $\text{Li}_{1.1}\text{Y}_{0.1}\text{Zr}_{1.9}(\text{PO}_4)_3$ after contact with the lithium metal increases the wettability of the pellet by the metallic lithium anode. Moreover, the $\text{Li}_{1.1}\text{Y}_{0.1}\text{Zr}_{1.9}(\text{PO}_4)_3$ pellet shows a relatively small interfacial resistance in symmetric Li/Li and all-solid-state Li-metal cells, providing these cells a small overpotential and a long cycling life.

Keywords: NASICON; hot pressing; interfacial resistance; Li-ion conductivity; all-solid-state batteries

1. Introduction

Rechargeable Li-metal batteries with a high-voltage cathode and Li-metal as an anode have much higher energy density than conventional rechargeable Li-ion batteries with a graphite anode. However, the Li-metal batteries have serious safety issues, because of the fast lithium dendrite formation and growth during charge; moreover, the limited chemical/electrochemical stability of the liquid organic electrolyte when the cell is operated at high temperatures and high voltages can result in the failure or even the explosion of the batteries [1–4]. Compared with liquid organic electrolytes, solid electrolytes have high mechanical strength and good thermal stability, and some solid electrolytes have similar Li-ion conductivities to the liquid electrolytes [5–7]. Moreover, the good wetting ability of the solid electrolyte by the metallic lithium anode can reduce or even remove the lithium dendrite formation in all-solid-state Li-metal batteries [8–10]. Therefore, developing all-solid-state Li-metal batteries by replacing the liquid electrolyte with a high Li-ion conductive solid-state electrolyte is one of the most effective strategies to improve the safety and energy density of the batteries.

Research on solid electrolytes is focusing on polymer electrolytes, ceramic electrolytes, and polymer/composite electrolytes. Ceramic electrolytes usually have higher Li-ion conductivities than polymer and polymer/composite electrolytes because of the slow chain motion of the polymer at room temperature [11–13]. The ceramic electrolytes also have much better mechanical strength

than the polymer electrolyte. Two kinds of ceramic electrolytes, including oxide and sulfide ceramics, are promising candidates in all-solid-state Li-metal batteries. Compared with the sulfide ceramics, the oxide ceramics show a larger electrochemical window, a much better stability in air, and a much lower cost. Oxide garnet-type (e.g., $\text{Li}_7\text{La}_3\text{Zr}_2\text{O}_{12}$) [14–19], NASICON-type (e.g., $\text{Li}_{1+x}\text{MxTi}_{2-x}(\text{PO}_4)_3$, $\text{M} = \text{Al}, \text{Ge}$) [20–26], perovskite-type (e.g., $\text{Li}_{3x}\text{La}_{(2/3)-x}\square_{(1/3)-2x}\text{TiO}_3$) [27–31], and antiperovskite-type electrolytes (e.g., Li_2OHX , $\text{X} = \text{Cl}, \text{Br}$) [32–38] have been reported to have high Li-ion conductivities at room temperature because of the suitable Li-ion transport channel inside the framework. Garnet and antiperovskite electrolytes are reported to be unstable in moist air, and the reaction between them and moisture destroys the structure, reduces the Li-ion conductivity of the solid electrolyte, and significantly increases Li-ion resistance across the interface [39–41]. Perovskite electrolytes and commercial NASICON electrolytes contain Ti^{4+} ions which are unstable at low voltages less than 2 V, although both of them are reported to be stable in water [42]. Replacing the Ti^{4+} by other stable metal ions may improve the stability of the perovskite and NASICON electrolytes with lithium metal. However, NASICON-type $\text{LiZr}_2(\text{PO}_4)_3$ presents a complex polymorphic behavior upon synthesis [43,44]. Four different crystalline forms (α' and α , β' and β phase), depending on different annealing procedures, have been reported [45,46]. The rhombohedral α phase with a space group R-3c prepared at high temperature transfers to the triclinic α' phase at temperatures < 60 °C. The orthorhombic β phase prepared at low temperature transfers to the monoclinic β' phase with a space group of $\text{P}2_1/\text{n}$ at 300 °C. Only the rhombohedral α phase of $\text{LiZr}_2(\text{PO}_4)_3$ is reported to have a high ionic conductivity above $10^{-5} \text{ S cm}^{-1}$ at 50 °C. However, the rhombohedral phase changes to the triclinic phase at room temperature, which has a much lower Li-ion conductivity of $10^{-7} \text{ S cm}^{-1}$.

In this work, we investigated the structural, chemical, and electrochemical stabilities of Y^{3+} -doped $\text{LiZr}_2(\text{PO}_4)_3$ by changing the Y^{3+} concentration; the structural stability of the sample was also characterized with XRD from -30 to 150 °C. We also tried different sintering technologies to study the influence of density on the electrochemical performance of the pellet. Different cells, including the symmetric Li/Li cell and Li/LiFePO₄ cell, were prepared to study the performance of the NASICON electrolyte in a battery and also to study ionic transport at the electrolyte/electrode interface. Y^{3+} doping in $\text{LiZr}_2(\text{PO}_4)_3$ was effective in improving the structural stability at a wide temperature range. A high Li-ion conductivity of $9 \times 10^{-5} \text{ S cm}^{-1}$ at room temperature was obtained for the sample prepared by hot pressing, which is much higher than the conductivity of the pellet prepared by spark plasma sintering [47]. The XPS depth profiles revealed that a passivation layer with a thickness of less than 100 nm formed on the surface of the pellet, which improved the cycling of the symmetric cell.

2. Experimental

For preparing $\text{Li}_{1+x}\text{Y}_x\text{Zr}_{2-x}(\text{PO}_4)_3$ ($0 \leq x \leq 0.2$), stoichiometric LiNO_3 (20% excess, Sinopharm, 4N, Beijing, China), $\text{Y}(\text{NO}_3)_3 \cdot 6\text{H}_2\text{O}$ (Sinopharm, 4N, Beijing, China), $\text{Zr}(\text{NO}_3)_4 \cdot 5\text{H}_2\text{O}$ (Sinopharm, AR, Beijing, China), $(\text{NH}_4)_2\text{HPO}_4$ (Sinopharm, 4N, Beijing, China) and citric acid (Aladdin, AR, Shanghai China) raw materials were dissolved in 100 mL deionized water and thoroughly mixed with a magnetic stirrer at 80 °C to obtain a homogeneous solution. A precursor was obtained after evaporating the solution at 70 °C. The obtained mixture was heated at 900 °C for 6 h to remove the absorbed water and decompose the phosphates and nitrates in the precursor. The precursor was then ball-milled in a planetary mill (Fritsch, Pulverisette 4, Pittsboro, United States) with anhydrous isopropanol at 300 rpm min^{-1} for 8 h, and the powders were dried and subsequently pressed into a pellet with a diameter of 10 mm. $\text{Li}_{1+x}\text{Y}_x\text{Zr}_{2-x}(\text{PO}_4)_3$ pellets were fired at 1150 °C for 12 h [48–50]. A Pt crucible was used to prepare the samples in a box furnace. Highly dense pellets were achieved by hot-pressing (ZT-40-20YB, Shanghai Chen Hua Electric Furnace Co. Ltd., Shanghai, China) at 1100–1250 °C for 3 h with an applied pressure of 50 Mpa. The finally obtained pellets were cut into pieces with a thickness of 500 μm for further electrochemical testing. The density of the pellet was obtained by dividing the mass by the volume of the pellet. Powder X-ray diffraction (XRD) patterns for the as-prepared samples were characterized with a Bruker-AXS D8-A25 (Billerica, United States) Advance diffractometer using $\text{Cu}_{\text{K}\alpha}$

radiation. The XRD pattern was collected from 10 to 60 degrees, with a step size of 0.02 degree; the lattice parameters of the obtained samples were obtained with JADE software. The phase compositions of the NASICON pellets with different Y^{3+} concentrations were obtained by refining the XRD data of the samples with Fullprof software (Version: Sep-2019); the lattice parameters, the shape parameters of the peaks, and the full width at half maximum (FWHM) parameters were refined. Scanning electron microscopy (SEM) and Energy-dispersive X-Ray spectroscopy (EDS) images were examined by a field-emission scanning electron microscopy (SEM, FEI Quanta 650, Hillsboro, United States). The impedance spectra of $Li_{1+x}Y_xZr_{2-x}(PO_4)_3$ ($0.1 \leq x \leq 0.2$) were collected with a precision impedance analyzer (Agilent 4294A, Santa Clara, United States) in the temperature range of 298–423 K and fitted by the equivalent circuit $(R_gCPE_g)(R_{gb}CPE_{gb})CPE$. The applied frequency was 110 MHz–40 Hz with an AC amplitude of 10 mV. X-ray photoelectron spectrometer (XPS) spectra (ESCALAB250Xi, ThermoFisher Scientific, Waltham, United States) of Li, O, Zr, P elements were characterized to monitor the interfacial reaction of Li/NASICON using a VG ESCALAB MKII spectrometer with an Al Ka monochromatic X-ray source. An Ar ion gun was used to etch at a sputtering rate of 25 nm min^{-1} .

$LY_{0.1}ZP$ pellets prepared by hot pressing were used for all the battery testing. For the symmetric cell testing, two lithium foils (0.5 cm^2) were put on both sides of the pellet, and the cell was cycled at a current density of 0.05 mA cm^{-2} with a duration time of 1 h at $60 \text{ }^\circ\text{C}$. The symmetric Li/ $LY_{0.1}ZP$ /Li cell after cycling for 80 h was disassembled in the glovebox, and the small pieces from the broken $LY_{0.1}ZP$ pellet were transferred to the SEM equipment for SEM and EDS mapping measurements. The lithium foil had a thickness of $100 \text{ }\mu\text{m}$ and a surface area of 0.5 cm^2 . One layer of Ni foam was put on top of the lithium foil to maintain good contact between lithium foil and the pellet. For the all-solid-state battery, the $LiFePO_4$ cathode was prepared by mixing $LiFePO_4$, carbon, PEO, and LiTFSI salt in acetonitrile with a weight ratio of 70:10:13:7. The cathode was dried in the oven at $80 \text{ }^\circ\text{C}$ for 24 h to remove the liquid acetonitrile. The slurry was coated on the aluminum foil by a doctor blade, and the loading of the active material was 3 mg cm^{-2} . The Li/ $LiFePO_4$ cell was cycled between 3.8 and 2.8 V at $60 \text{ }^\circ\text{C}$. In all-solid-state Li/ $LiFePO_4$ cells, the lithium and $Li_{1+x}Y_xZr_{2-x}(PO_4)_3$ pellets were separated by a solid polymer to reduce the interfacial resistance. The polymer was prepared by mixing PEO (M_w : 600,000) and Lithium bis(trifluoromethanesulfonyl)imide (LiTFSI) with an EO/Li⁺ ratio of 10 in acetonitrile. The solution was stirred overnight and cast on a polytetrafluoroethylene dish. The polymer electrolyte was dried at $60 \text{ }^\circ\text{C}$ for 48 h. The impedances of the symmetric cell and the all-solid-state cell were measured in an Autolab working station (Herisau, Switzerland) with frequencies from 1 MHz to 1 Hz. The cycling of the battery testing was conducted in land battery test systems (CT2001A, Wuhan, China).

3. Results and Discussion

The XRD patterns of as-synthesized powders in a regular box furnace were compared in Figure 1a; dopant-free $LiZr_2(PO_4)_3$ exhibited a monoclinic phase at room temperature, which is consistent with a previous report [46]. The pellet with a rhombohedral structure was obtained with Y^{3+} doping; all the diffraction peaks for $Li_{1+x}Y_xZr_{2-x}(PO_4)_3$ ($x = 0.1$ and 0.15) samples can be indexed to R-3c group. Some impurities existed in the sample with $x = 0.2$. The lattice parameters of the sample increased with increasing Y^{3+} concentration because of the larger ionic size of Y^{3+} relative to Zr^{4+} , as shown in Figure S1. The XRD results of $Li_{1.1}Y_{0.1}Zr_{1.9}(PO_4)_3$ prepared by hot-pressing at 1100 – $1250 \text{ }^\circ\text{C}$ for 3 h are shown in Figure 1b. Hot-pressing treatment did not change the rhombohedral phase when the pellets were fired at temperatures above $1150 \text{ }^\circ\text{C}$. The small shoulder at 20 degrees in the sample with $x = 0.15$ and 0.2 indicates there may be minimal triclinic $LiZr_2(PO_4)_3$ in the pellet. The sample with $x = 0.1$ could be fitted well with the rhombohedral phase, and the sample with $x = 0.15$ and 0.2 could be refined well with the mixed rhombohedral and the triclinic phases (Figure S2). The contents of the triclinic phases in the samples with $x = 0.15$ and 0.2 were 3.5% and 29.2%, respectively. Increasing Y^{3+} ions also increased the triclinic phase, which reduces the ionic conductivity of the NASICON electrolyte. The SEM image in Figure 1c shows that $Li_{1+x}Y_xZr_{2-x}(PO_4)_3$ with $x = 0.1$ (denoted as

$\text{LiY}_{0.1}\text{ZP}$) was composed of particles with an average grain diameter of 2 μm . The relative density of $\text{LY}_{0.1}\text{ZP}$ pellets prepared by regular sintering was 76% and is further improved to 94% by hot-pressing (HP) (Figure S3). The pellet prepared by hot pressing showed some transgranular fractures, indicating the grain–boundary of the pellet has a higher mechanical strength. No closed pores and fewer grain boundaries can be observed in $\text{LY}_{0.1}\text{ZP}$ sintered by HP at 1200 $^{\circ}\text{C}$ for 3 h (Figure 1d and Figure S4). The reduced porosity and grain boundaries could improve Li-ion transfer at the grain boundaries.

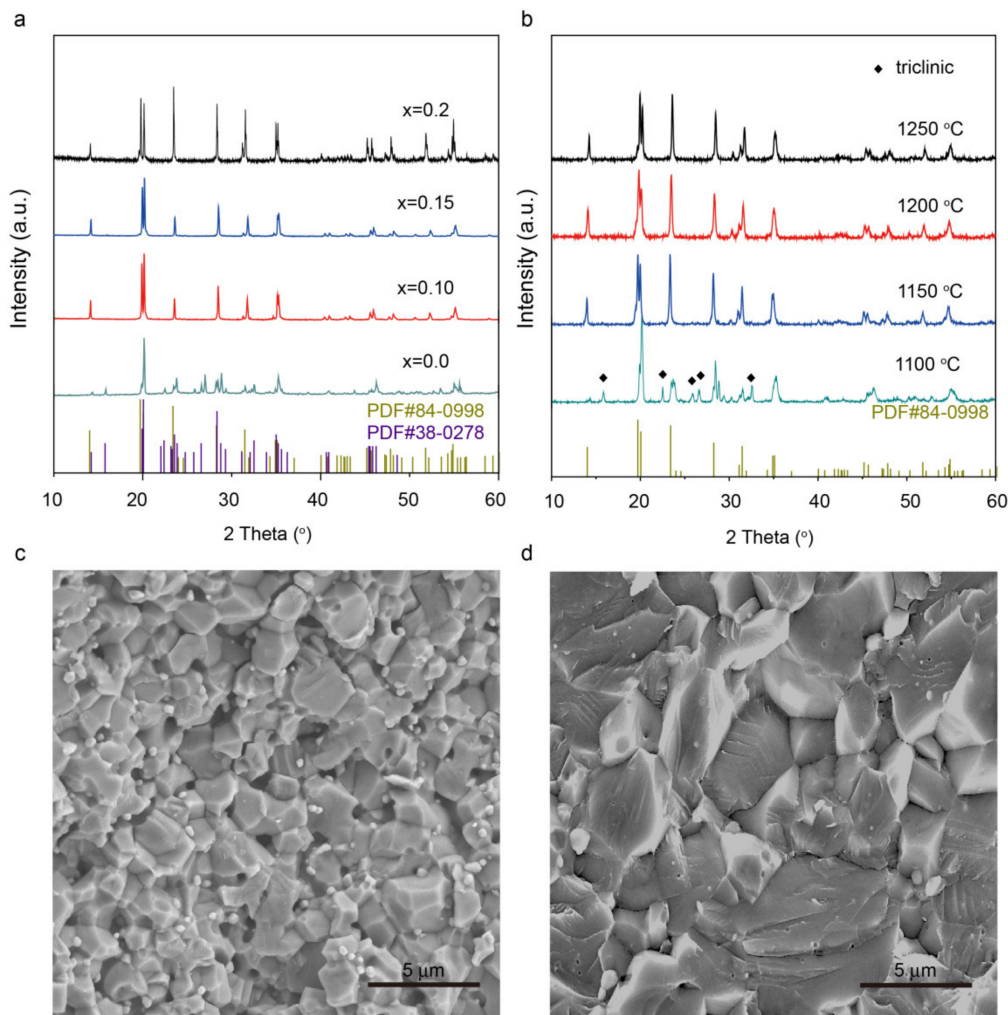


Figure 1. (a) XRD patterns of $\text{Li}_{1+x}\text{Y}_x\text{Zr}_{2-x}(\text{PO}_4)_3$ ($0 \leq x \leq 0.2$) electrolyte fired at 1150 $^{\circ}\text{C}$ for 12 h. (b) XRD patterns of $\text{LY}_{0.1}\text{ZP}$ treated by hot-pressing (HP) at 1100–1250 $^{\circ}\text{C}$. The cross-section SEM images of $\text{LY}_{0.1}\text{ZP}$ treated by (c) regular sintering and (d) hot-pressing. PDF #84-0998 and #38-0278 in (a) correspond to the rhombohedral and triclinic structure of $\text{LiZr}_2(\text{PO}_4)_3$, respectively.

To better understand the phase stabilization by Y^{3+} doping, phase composition vs. temperature was collected by in-situ powder X-ray diffraction (XRD). It can be seen from the XRD patterns in Figure 2a,b that characteristic peaks of the monoclinic phase in NASICON did not appear during heating from -30 to 150 $^{\circ}\text{C}$ and during the cooling process. It is evidenced that a high level of consistency with the characteristic rhombohedral α phase was obtained in a wide temperature range. There was no clear lattice parameter change during the heating and cooling process. The unit cell parameters of the as-prepared sample before heating ($V = 1480.00 \text{ \AA}^3$, $a = 8.8169 \text{ \AA}$, $c = 21.9834 \text{ \AA}$) and the heated samples (e.g. 150 $^{\circ}\text{C}$, $V = 1480.08 \text{ \AA}^3$, $a = 8.8111 \text{ \AA}$, $c = 22.01374 \text{ \AA}$) are almost identical. The lattice stabilization with only minor thermal expansion, for $\text{LY}_{0.1}\text{ZP}$, may benefit from a stronger bond strength of $\text{Y}^{3+}-\text{O}^{2-}$. It is reported that Y^{3+} doping can reduce the M1 site interstitial space and

increase the volume of M2' [43]; in our case the lattice parameter $a = 8.8111 \text{ \AA}$ for LY_{0.1}ZP shrank a little compared to LiZr₂(PO₄)₃ at 150 °C (8.8549 Å); this local lattice distortion gives rise to the enhancement of ionic conductivity. According to the literature, the $\alpha \rightarrow \alpha'$ transition of LiZr₂(PO₄)₃ is generally at 50 °C [44]. In our case, the pure rhombohedral α phase of LY_{0.1}ZP retained the structure at room temperature without the first-order transition. There is no phase deterioration, and the first-order transition from a rhombohedral α phase to a monoclinic phase occurs even at $-30 \text{ }^\circ\text{C}$, showing an effective structural stabilization by Y³⁺ doping.

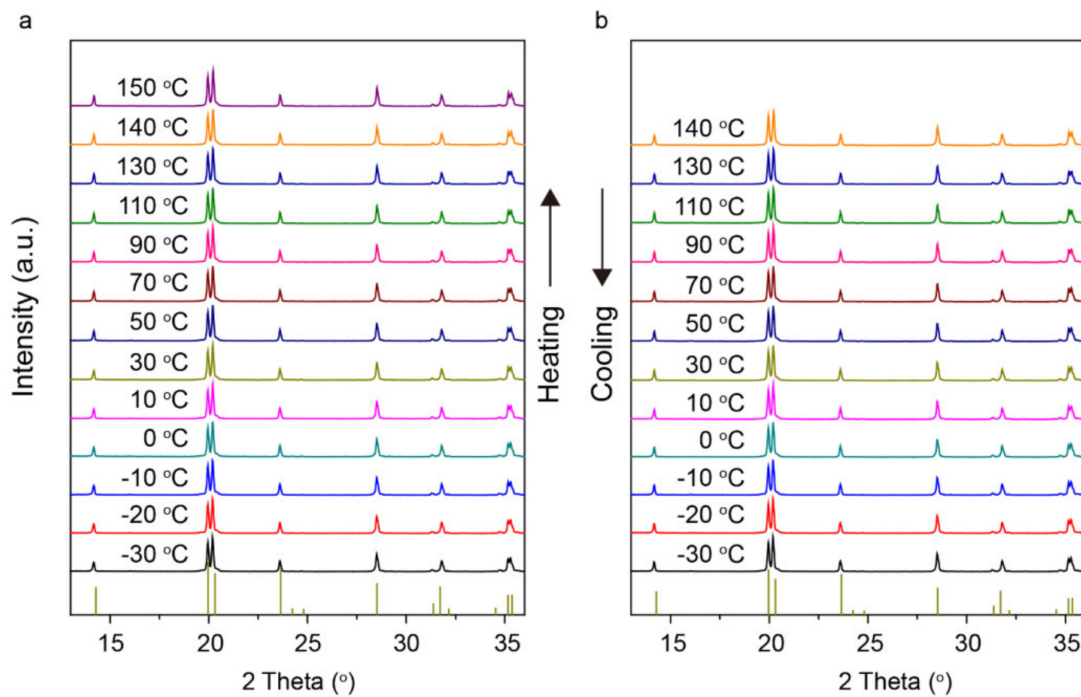


Figure 2. XRD patterns for the as-prepared LY_{0.1}ZP electrolyte from -30 to $150 \text{ }^\circ\text{C}$: (a) during the heating and (b) the cooling process.

The impedance spectra of the Li_{1+x}Y_xZr_{2-x}(PO₄)₃ ($0.1 \leq x \leq 0.2$) pellets prepared by regular sintering and hot pressing are shown in Figure 3 and Figure S5. The curves show two semicircles at the high and low frequency, which correspond to Li-ion transfer in the bulk and grain boundary of the pellet. The bulk and grain-boundary resistance could be obtained by fitting the experimental data with a conventional equivalent circuit consisting of $(R_g \text{CPE}_g)(R_{gb} \text{CPE}_{gb})\text{CPE}$. For the samples prepared by regular sintering, the LY_{0.1}ZP pellet showed the highest bulk and total Li-ion conductivity of $4.5 \times 10^{-5} \text{ S cm}^{-1}$, respectively; the samples with $x = 0.15$ and 0.2 have a lower ionic conductivity than the sample with $x = 0.1$, which may be caused by the impurities in the samples with increasing Y³⁺ concentration. The total Li-ion conductivity of the pellet prepared by hot-pressing was improved to $9 \times 10^{-5} \text{ S cm}^{-1}$ at room temperature. Hot-pressing significantly reduced the grain boundary resistance of the LY_{0.1}ZP pellet, and the total ionic conductivity of the pellet prepared by hot-pressing is two orders of magnitude higher than that of LiZr₂(PO₄)₃ without doping. Enhancement in Li-ion conductivity can be explained by (1) the increasing concentration of lithium ions and (2) the shrinkage of the M1 cavity and the expansion of the M2 space with Y³⁺ doping, which provide a shorter Li1- Li1' hopping distance and lower bond strength for Li2 along the Li1-Li2 pathway [43]. Li-ion conductivities as a function of temperature in the range of $30\text{--}150 \text{ }^\circ\text{C}$ were collected, and a linear Arrhenius behavior was observed (Figure 3b); the rhombohedral LY_{0.1}ZP had a small activation energy of 0.34 eV , indicating a fast Li-ion transfer in the NASICON framework.

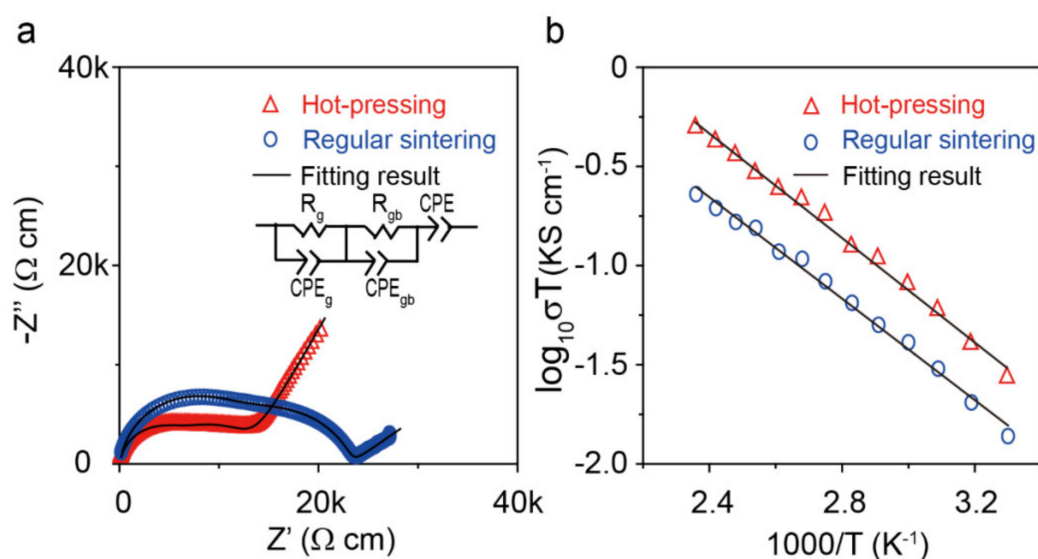


Figure 3. (a) Li-ion conductivities of LY_{0.1}ZP at room temperature. The applied frequency was 110 MHz–40 Hz. and (b) Arrhenius plots of LY_{0.1}ZP prepared by regular sintering and hot-pressing; the Arrhenius plots are based on the total impedances of the pellets.

The electrochemical stability of LY_{0.1}ZP with lithium metal was studied by assembling in a symmetric cell. The LY_{0.1}ZP electrolyte prepared by hot pressing shows an interfacial resistance with lithium metal of 392 Ω cm² at 60 °C (Figure 4a), which is comparable with Ge-coated LAGP [51]. A fixed current density of 0.05 mA cm⁻² was used to evaluate the reversibility of the Li plating and stripping process of LY_{0.1}ZP in the symmetric cell. The resulting galvanostatic profile is shown in Figure 4b; a polarization voltage of 0.1 V with a negligible variation was observed within 80 h. The SEM images in Figure 4c,d exhibit a uniform wetting layer on LY_{0.1}ZP after contact with lithium metal. The cross-section image and the EDS mapping of the LY_{0.1}ZP in Figure 4e and Figure S6 show that the LY_{0.1}ZP maintained good compactness, and the passivation product was a glassy phase that wet well on the LY_{0.1}ZP surface. A glassy interphase layer leads to good contact between the electrode and electrolyte. The pathway of Li⁺ ions across the Li/NASICON interface is continuous, resulting in a small interfacial resistance. The mapping images confirmed that the interfacial area had a homogenous distribution of Zr, P, Li and O elements.

To further identify the composition distribution at the interface area, XPS depth profiles were collected. Figure S7 presents the atomic concentration distribution along with the depth from the top section. The content of O, Li, P, Zr elements in LY_{0.1}ZP after cycling in the symmetric cell remained almost unchanged within the recorded depth, which agrees well with the EDS mapping results. Detailed analysis of the P 2p spectrum (Figure 5a) indicates that the top interface consists of PO₄³⁻ (135 eV) and P³⁻ (129 eV) signals, which are contributed from PO₄³⁻ tetrahedral and Li₃P, respectively. The peak corresponding to Li₃P disappeared after full removal of the top layer (~100 nm). LY_{0.1}ZP reacts with lithium metal to form a Li₃P layer with a thickness of 50 nm, and the reaction increases the contact between lithium metal and LY_{0.1}ZP; the good ionic conductivity of the Li₃P layer could help improve the wettability of the LY_{0.1}ZP pellet by the metallic lithium anode. Figure 5b indicates the related shift of Li 1s peak. Peak splitting attributable to local an oxygen coordination change from bridging PO₄³⁻ to nonbridging P-O-P was found in the O 1s spectra at 533 and 531 eV, indicating the P⁴⁺-O²⁻ bond breakage at the surface. Meanwhile, the peak at 531.6 eV is ascribed to the O²⁻ 2p binding energy in LY_{0.1}ZP. The presence of P³⁻, the change of O 2s, and the Li 1s on the LY_{0.1}ZP surface suggest the self-compatibility process of LY_{0.1}ZP cycled in the Li/Li symmetric cell.

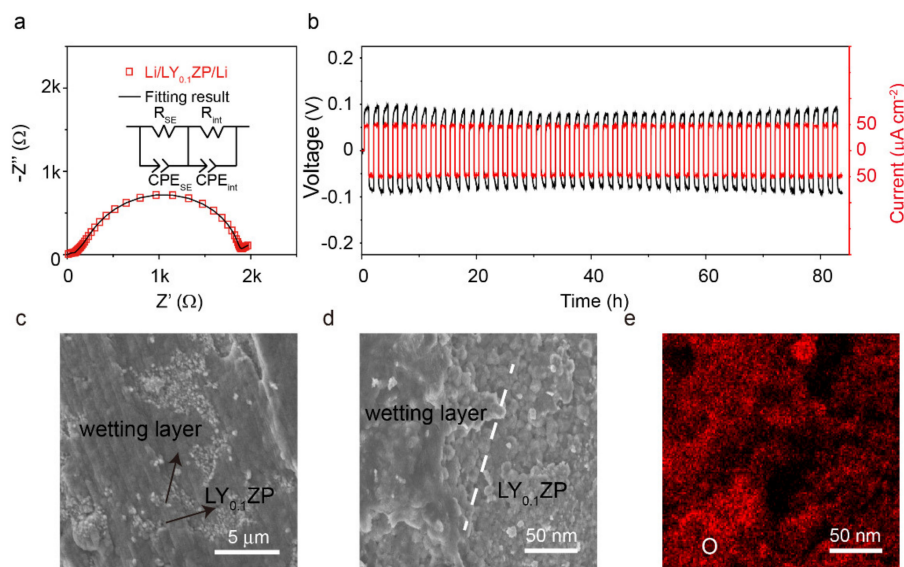


Figure 4. (a) Impedance plot of a symmetric Li/LY0.1ZP/Li cell tested at 60 °C; the applied frequency for the symmetric cell was 1 MHz–1 Hz. (b) The cycling stability of LY0.1ZP electrolytes in a symmetric Li/LY0.1ZP/Li cell at 0.05 mA cm⁻² at 60 °C. (c) The top view and (d) cross-section images of LY0.1ZP after contacting with lithium metal. (e) The mapping of O element on cycled LY0.1ZP. Scale bar: 50 nm; the size of the Li foil was 0.5 cm⁻².

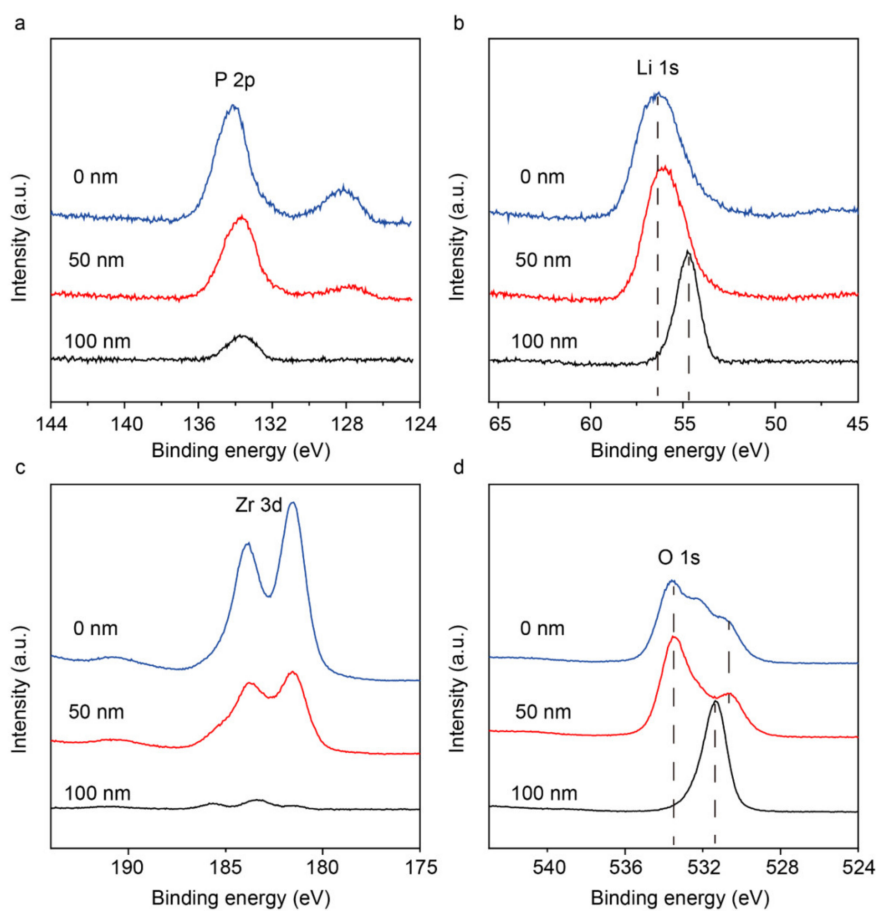


Figure 5. The XPS spectra of LY0.1ZP cycled in a Li/Li cell. The evolution profiles of relative (a) P, (b) Li, (c) Zr, (d) O elemental intensities along the depth direction. The separation distance was 50 nm, calculated from the Ar sputtering.

The performance of $\text{LY}_{0.1}\text{ZP}$ in all-solid-state Li-metal batteries with a composite LiFePO_4 cathode was studied. To further reduce the $\text{Li}/\text{LY}_{0.1}\text{ZP}$ interfacial resistance, and to improve the cycling performance of the cell, a Li-ion conducting polymer was put between the lithium metal anode and the $\text{LY}_{0.1}\text{ZP}$ solid electrolyte, which is similar to other reports [30]. The obtained $\text{Li}/\text{Polymer}/\text{LY}_{0.1}\text{ZP}/\text{LFP}$ solid-state cell had a total resistance of 2200Ω at 60°C (Figure 6a). Figure 6b is the charge/discharge voltage profile of the all-solid-state battery at current densities of 0.05 mA cm^{-2} (about 0.1C); the cell showed a flat voltage plateau during charge/discharge with a small overpotential of 0.15 V at 0.05 mA cm^{-2} . The discharge capacity of the cell was 130 mAh g^{-1} and a 119 mAh g^{-1} capacity was retained after 100 cycles (Figure 6c). The all-solid-state cell had a high coulombic efficiency of 99.5% during cycling, indicating a stable $\text{LY}_{0.1}\text{ZP}/\text{cathode}$ interface.

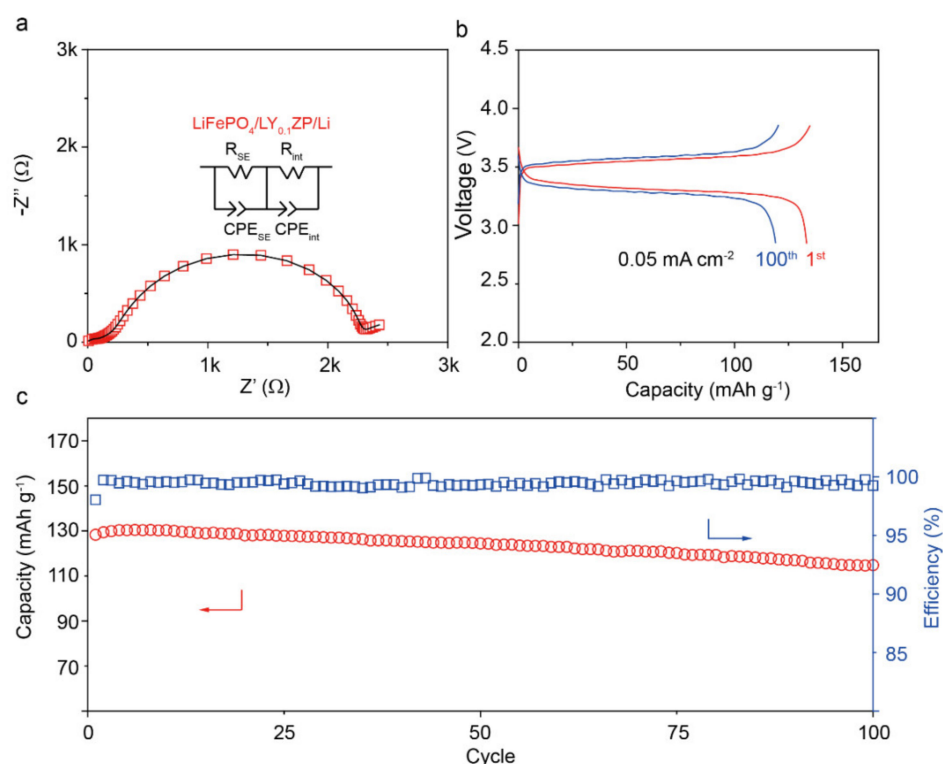


Figure 6. (a) Impedance profile of the all-solid-state $\text{LiFePO}_4/\text{LY}_{0.1}\text{ZP}/\text{Li}$ cell at 60°C . (b) Charge and discharge voltage profiles and (c) cycling performance of the all-solid-state $\text{LiFePO}_4/\text{LY}_{0.1}\text{ZP}/\text{Li}$ cell at 60°C . The size of the LiFePO_4 was 0.5 cm^{-2} .

4. Conclusions

Rhombohedral $\text{LiZr}_2(\text{PO}_4)_3$ phase was stabilized by Y^{3+} doping, and the $\text{Li}_{1.1}\text{Y}_{0.1}\text{Zr}_{1.9}(\text{PO}_4)_3$ showed a high density and a high Li-ion conductivity of $9 \times 10^{-5} \text{ S cm}^{-1}$ at room temperature, which is two orders magnitude higher than that of $\text{LiZr}_2(\text{PO}_4)_3$. The absence of a phase transition of $\text{Li}_{1.1}\text{Y}_{0.1}\text{Zr}_{1.9}(\text{PO}_4)_3$ from rhombohedral to triclinic at -30°C showed the excellent structural stabilization by Y^{3+} doping. With the formation of a self-wetting layer at the $\text{LY}_{0.1}\text{ZP}/\text{Li}$ interface, highly reversible dendrite-free Li plating/stripping at a current density of 0.05 mA cm^{-2} was achieved. Moreover, the $\text{Li}_{1.1}\text{Y}_{0.1}\text{Zr}_{1.9}(\text{PO}_4)_3$ pellet showed a relatively small interfacial resistance in symmetric Li/Li and all-solid-state Li-metal cells. The long-term cycling performance of the all-solid-state cell demonstrates that $\text{Li}_{1.1}\text{Y}_{0.1}\text{Zr}_{1.9}(\text{PO}_4)_3$ prepared by hot-pressing is a promising candidate for all-solid-state Li-metal batteries.

Supplementary Materials: The following are available online at <http://www.mdpi.com/1996-1944/13/7/1719/s1>, Figure S1: The lattice parameters of the sample with (a) different Y^{3+} concentration and (b) different temperatures, Figure S2: The refinement of the XRD data of $\text{Li}_{1+x}\text{Y}_x\text{Zr}_{2-x}(\text{PO}_4)_3$ ($0.1 \leq x \leq 0.2$). The green and yellow

vertical lines are the Braga positions of the rhombohedral and triclinic phases, respectively. The red circle and the black line is the experimental data and the fitting result, respectively. The small χ^2 value indicates a good fitting, Figure S3: Relative densities of $\text{Li}_{1+x}\text{Y}_x\text{Zr}_{2-x}(\text{PO}_4)_3$ ($0.1 \leq x \leq 0.2$) pellets treated by regular sintering and hot-pressing from 1100 to 1250 °C, Figure S4: SEM images of $\text{LY}_{0.1}\text{ZP}$ pellets prepared by hot-pressing from 1100 to 1250 °C, Figure S5: Nyquist plots of $\text{Li}_{1+x}\text{Y}_x\text{Zr}_{2-x}(\text{PO}_4)_3$ ($0.1 \leq x \leq 0.2$) pellets prepared by regular sintering and hot-pressing, Figure S6: EDS images of P, Zr, Y elements distribution on cycled $\text{LY}_{0.1}\text{ZP}$ in a Li/Li cell, Figure S7: Atomic percentages along with the depth of cycled $\text{LY}_{0.1}\text{ZP}$ in a Li/Li cell.

Author Contributions: B.H. and X.Y. conceived the idea and designed the research. Q.L. and C.X. prepared the samples and did all the characterization. All authors analyzed the results and commented on the paper. Q.L. and B.H. wrote the paper. All authors have read and agreed to the published version of the manuscript.

Funding: This research was funded by the Nation Natural Science Foundation of China (NSFC-No. 51872159 and 51572145).

Conflicts of Interest: The authors declare no conflict of interest.

References

1. Goodenough, J.B.; Kim, Y. Challenges for rechargeable Li batteries. *Chem. Mater.* **2010**, *22*, 587–603. [[CrossRef](#)]
2. Etacheri, V.; Marom, R.; Elazari, R.; Salitra, G.; Aurbach, D. Challenges in the development of advanced Li-ion batteries: A review. *Energy Environ. Sci.* **2011**, *4*, 3243–3262. [[CrossRef](#)]
3. Goodenough, J.B.; Park, K.-S. The Li-ion rechargeable battery: A perspective. *J. Am. Chem. Soc.* **2013**, *135*, 1167–1176. [[CrossRef](#)] [[PubMed](#)]
4. Tarascon, J.-M.; Armand, M. Issues and challenges facing rechargeable lithium batteries. *Mater. Sustain. Energy A Collect. Peer Rev. Res. Rev. Artic. Nat. Publ. Group* **2010**, 171–179. [[CrossRef](#)]
5. Manthiram, A.; Yu, X.; Wang, S. Lithium battery chemistries enabled by solid-state electrolytes. *Nat. Rev. Mater.* **2017**, *2*, 1–16.
6. Gao, Z.; Sun, H.; Fu, L.; Ye, F.; Zhang, Y.; Luo, W.; Huang, Y. Promises, challenges, and recent progress of inorganic solid-state electrolytes for all-solid-state lithium batteries. *Adv. Mater.* **2018**, *30*, 1705702. [[CrossRef](#)]
7. Zhao, N.; Khokhar, W.; Bi, Z.; Shi, C.; Guo, X.; Fan, L.-Z.; Nan, C.-W. Solid garnet batteries. *Joule* **2019**, *3*, 1190–1199. [[CrossRef](#)]
8. Li, Y.; Zhou, W.; Chen, X.; Lü, X.; Cui, Z.; Xin, S.; Xue, L.; Jia, Q.; Goodenough, J.B. Mastering the interface for advanced all-solid-state lithium rechargeable batteries. *Proc. Natl. Acad. Sci. USA* **2016**, *113*, 13313–13317. [[CrossRef](#)]
9. Xin, S.; You, Y.; Wang, S.; Gao, H.-C.; Yin, Y.-X.; Guo, Y.-G. Solid-state lithium metal batteries promoted by nanotechnology: Progress and prospects. *ACS Energy Lett.* **2017**, *2*, 1385–1394. [[CrossRef](#)]
10. Luo, W.; Gong, Y.; Zhu, Y.; Fu, K.K.; Dai, J.; Lacey, S.D.; Wang, C.; Liu, B.; Han, X.; Mo, Y.; et al. Transition from superlithiophobicity to superlithiophilicity of garnet solid-state electrolyte. *J. Am. Chem. Soc.* **2016**, *138*, 12258–12262. [[CrossRef](#)]
11. Stephan, A.M. Review on gel polymer electrolytes for lithium batteries. *Eur. Polym. J.* **2006**, *42*, 21–42. [[CrossRef](#)]
12. Stephan, A.M.; Nahm, K.S. Review on composite polymer electrolytes for lithium batteries. *Polymer* **2006**, *47*, 5952–5964. [[CrossRef](#)]
13. Quartarone, E.; Mustarelli, P.; Magistris, A. PEO-based composite polymer electrolytes. *Solid State Ion* **1998**, *110*, 1–14. [[CrossRef](#)]
14. Murugan, R.; Thangadurai, V.; Weppner, W. Fast lithium ion conduction in garnet-type $\text{Li}_7\text{La}_3\text{Zr}_2\text{O}_{12}$. *Angew. Chem. Int. Ed.* **2007**, *46*, 7778–7781. [[CrossRef](#)] [[PubMed](#)]
15. Thangadurai, V.; Narayanan, S.; Pinzaru, D. Garnet-type solid-state fast Li ion conductors for Li batteries: Critical review. *Chem. Soc. Rev.* **2014**, *43*, 4714–4727. [[CrossRef](#)] [[PubMed](#)]
16. Li, Y.; Han, J.-T.; Wang, C.-A.; Xie, H.; Goodenough, J.B. Optimizing Li^+ conductivity in a garnet framework. *J. Mater. Chem.* **2012**, *22*, 15357–15361. [[CrossRef](#)]
17. Liu, J.; Gao, X.; Hartley, G.O.; Rees, G.J.; Gong, C.; Richter, F.H.; Janek, J.; Xia, Y.; Robertson, A.W.; Johnson, L.R. The Interface between $\text{Li}_{6.5}\text{La}_3\text{Zr}_{1.5}\text{Ta}_{0.5}\text{O}_{12}$ and Liquid Electrolyte. *Joule* **2020**, *4*, 101–108. [[CrossRef](#)]
18. Feng, W.; Dong, X.; Zhang, X.; Lai, Z.; Li, P.; Wang, C.; Wang, Y.; Xia, Y. Li/Garnet Interface Stabilization by Thermal-Decomposition Vapor Deposition of an Amorphous Carbon Layer. *Angew. Chem. Int. Ed.* **2020**, *59*, 5346–5349. [[CrossRef](#)]

19. Chi, S.-S.; Liu, Y.; Zhao, N.; Guo, X.; Nan, C.-W.; Fan, L.-Z. Solid polymer electrolyte soft interface layer with 3D lithium anode for all-solid-state lithium batteries. *Energy Storage Mater.* **2019**, *17*, 309–316. [[CrossRef](#)]
20. Aono, H.; Sugimoto, E.; Sadaoka, Y.; Imanaka, N.; Adachi, G.-Y. The electrical properties of ceramic electrolytes for $\text{LiM}_x\text{Ti}_{2-x}(\text{PO}_4)_{3+y}\text{Li}_2\text{O}$, $\text{M} = \text{Ge, Sn, Hf, and Zr}$ systems. *J. Electrochem. Soc.* **1993**, *140*, 1827–1833. [[CrossRef](#)]
21. Aono, H.; Sugimoto, E.; Sadaoka, Y.; Imanaka, N.; Adachi, G.-Y. Electrical properties and crystal structure of solid electrolyte based on lithium hafnium phosphate $\text{LiHf}_2(\text{PO}_4)_3$. *Solid State Ion.* **1993**, *62*, 309–316. [[CrossRef](#)]
22. Aono, H.; Imanaka, N.; Adachi, G.-Y. High Li^+ conducting ceramics. *Acc. Chem. Res.* **1994**, *27*, 265–270. [[CrossRef](#)]
23. Wu, N.; Chien, P.H.; Li, Y.; Dolocan, A.; Xu, H.; Xu, B.; Grundish, N.S.; Jin, H.; Hu, Y.-Y.; Goodenough, J.B. Fast Li^+ conduction mechanism and interfacial chemistry of a NASICON/polymer composite electrolyte. *J. Am. Chem. Soc.* **2020**, *142*, 2497–2505. [[CrossRef](#)] [[PubMed](#)]
24. Bonizzoni, S.; Ferrara, C.; Berbenni, V.; Anselmi-Tamburini, U.; Mustarelli, P.; Tealdi, C. NASICON-type polymer-in-ceramic composite electrolytes for lithium batteries. *Phys. Chem. Chem. Phys.* **2019**, *21*, 6142–6149. [[CrossRef](#)]
25. Hou, M.; Liang, F.; Chen, K.; Dai, Y.; Xue, D. Challenges and perspectives of NASICON-type solid electrolytes for all-solid-state lithium batteries. *Nanotechnology* **2019**, *31*, 132003. [[CrossRef](#)]
26. Liang, Y.; Peng, C.; Kamiike, Y.; Kuroda, K.; Okido, M. Gallium doped NASICON type $\text{LiTi}_2(\text{PO}_4)_3$ thin-film grown on graphite anode as solid electrolyte for all solid state lithium batteries. *J. Alloy. Compd.* **2019**, *775*, 1147–1155. [[CrossRef](#)]
27. Knauth, P. Inorganic solid Li ion conductors: An overview. *Solid State Ion.* **2009**, *180*, 911–916. [[CrossRef](#)]
28. Wu, J.; Chen, L.; Song, T.; Zou, Z.; Gao, J.; Zhang, W.; Shi, S. A review on structural characteristics, lithium ion diffusion behavior and temperature dependence of conductivity in perovskite-type solid electrolyte $\text{Li}_{3-x}\text{La}_{2/3-x}\text{TiO}_3$. *Funct. Mater. Lett.* **2017**, *10*, 1730002. [[CrossRef](#)]
29. Huang, B.; Xu, B.; Li, Y.; Zhou, W.; You, Y.; Zhong, S.; Wang, C.-A.; Goodenough, J.B. Li-ion conduction and stability of perovskite $\text{Li}_{3/8}\text{Sr}_{7/16}\text{Hf}_{1/4}\text{Ta}_{3/4}\text{O}_3$. *ACS Appl. Mater. Interfaces* **2016**, *8*, 14552–14557. [[CrossRef](#)]
30. Li, Y.; Xu, H.; Chien, P.H.; Wu, N.; Xin, S.; Xue, L.; Park, K.; Hu, Y.Y.; Goodenough, J.B. A perovskite electrolyte that is stable in moist air for lithium-ion batteries. *Angew. Chem. Int. Ed.* **2018**, *57*, 8587–8591. [[CrossRef](#)]
31. Stramare, S.; Thangadurai, V.; Weppner, W. Lithium lanthanum titanates: A review. *Chem. Mater.* **2003**, *15*, 3974–3990. [[CrossRef](#)]
32. Zhao, Y.; Daemen, L.L. Superionic conductivity in lithium-rich anti-perovskites. *J. Am. Chem. Soc.* **2012**, *134*, 15042–15047. [[CrossRef](#)] [[PubMed](#)]
33. Li, Y.; Zhou, W.; Xin, S.; Li, S.; Zhu, J.; Lü, X.; Cui, Z.; Jia, Q.; Zhou, J.; Zhao, Y. Fluorine-doped Antiperovskite electrolyte for all-solid-state lithium-ion batteries. *Angew. Chem. Int. Ed.* **2016**, *55*, 9965–9968. [[CrossRef](#)] [[PubMed](#)]
34. Hood, Z.D.; Wang, H.; Samuthira Pandian, A.; Keum, J.K.; Liang, C. Li_2OHCl crystalline electrolyte for stable metallic lithium anodes. *J. Am. Chem. Soc.* **2016**, *138*, 1768–1771. [[CrossRef](#)] [[PubMed](#)]
35. Xu, H.; Xuan, M.; Xiao, W.; Shen, Y.; Li, Z.; Wang, Z.; Hu, J.; Shao, G. Lithium ion conductivity in double antiperovskite $\text{Li}_{6.5}\text{OS}_{15}\text{I}_{1.5}$: Alloying and boundary effects. *ACS Appl. Energy Mater.* **2019**, *2*, 6288–6294. [[CrossRef](#)]
36. Wu, M.; Xu, B.; Luo, W.; Sun, B.; Shi, J.; Ouyang, C. First-principles study on the structural, electronic, and Li-ion mobility properties of anti-perovskite superionic conductor Li_3OCl (100) surface. *Appl. Surf. Sci.* **2020**, *510*, 145394. [[CrossRef](#)]
37. Shen, K.; Wang, Y.; Zhang, J.; Zong, Y.; Li, G.; Zhao, C.; Chen, H. Revealing the effect of grain boundary segregation on Li ion transport in polycrystalline anti-perovskite Li_3ClO : a phase field study. *Phys. Chem. Chem. Phys.* **2020**, *22*, 3030–3036. [[CrossRef](#)]
38. Song, A.Y.; Turcheniuk, K.; Leisen, J.; Xiao, Y.; Meda, L.; Borodin, O.; Yushin, G. Understanding Li-Ion Dynamics in Lithium Hydroxide (Li_2OHCl) Solid State Electrolyte via Addressing the Role of Protons. *Adv. Energy Mater.* **2020**, *10*, 1903480. [[CrossRef](#)]
39. Li, Y.; Han, J.-T.; Vogel, S.C.; Wang, C.-A. The reaction of $\text{Li}_{6.5}\text{La}_3\text{Zr}_{1.5}\text{Ta}_{0.5}\text{O}_{12}$ with water. *Solid State Ion.* **2015**, *269*, 57–61. [[CrossRef](#)]
40. Shimonishi, Y.; Toda, A.; Zhang, T.; Hirano, A.; Imanishi, N.; Yamamoto, O.; Takeda, Y. Synthesis of garnet-type $\text{Li}_{7-x}\text{La}_3\text{Zr}_2\text{O}_{12-1/2x}$ and its stability in aqueous solutions. *Solid State Ion.* **2011**, *183*, 48–53. [[CrossRef](#)]
41. Schroeder, D.J.; Hubaud, A.A.; Vaughney, J.T. Stability of the solid electrolyte Li_3OBr to common battery solvents. *Mater. Res. Bull.* **2014**, *49*, 614–617. [[CrossRef](#)]

42. Zhao, Y.; Ding, Y.; Li, Y.; Peng, L.; Byon, H.R.; Goodenough, J.B.; Yu, G. A chemistry and material perspective on lithium redox flow batteries towards high-density electrical energy storage. *Chem. Soc. Rev.* **2015**, *44*, 7968–7996. [[CrossRef](#)] [[PubMed](#)]
43. Li, Y.; Liu, M.; Liu, K.; Wang, C.-A. High Li⁺ conduction in NASICON-type Li_{1+x}Y_xZr_{2-x}(PO₄)₃ at room temperature. *J. Power Sources* **2013**, *240*, 50–53. [[CrossRef](#)]
44. Catti, M.; Comotti, A.; Di Blas, S. High-temperature lithium mobility in α-LiZr₂(PO₄)₃ NASICON by neutron diffraction. *Chem. Mater.* **2003**, *15*, 1628–1632. [[CrossRef](#)]
45. Nomura, K.; Ikeda, S.; Ito, K.; Einaga, H. Ionic conduction behavior in zirconium phosphate framework. *Solid State Ion.* **1993**, *61*, 293–301. [[CrossRef](#)]
46. Arbi, K.; Ayadi-Trabelsi, M.; Sanz, J. Li mobility in triclinic and rhombohedral phases of the Nasicon-type compound LiZr₂(PO₄)₃ as deduced from NMR spectroscopy. *J. Mater. Chem.* **2002**, *12*, 2985–2990. [[CrossRef](#)]
47. Xu, H.; Wang, S.; Wilson, H.; Zhao, F.; Manthiram, A. Y-doped NASICON-type LiZr₂(PO₄)₃ solid electrolytes for lithium-metal batteries. *Chem. Mater.* **2017**, *29*, 7206–7212. [[CrossRef](#)]
48. Mariappan, C.R.; Kumar, P.; Kumar, A.; Indris, S.; Ehrenberg, H.; Prakash, G.V.; Jose, R. Ionic conduction and dielectric properties of yttrium doped LiZr₂(PO₄)₃ obtained by a Pechini-type polymerizable complex route. *Ceram. Int.* **2018**, *44*, 15509–15516. [[CrossRef](#)]
49. Stenina, I.; Kislitsyn, M.; Pinus, I.Y.; Haile, S.; Yaroslavtsev, A.B. Phase transitions and ion conductivity in NASICON-type compounds Li_{1+x}Zr_{2-x}M_x(PO₄)₃, M = Ta, Nb, Y, Sc, In. *Trans Tech Pub. Ltd.* **2006**, *249*, 255–262.
50. Xie, H.; Li, Y.; Goodenough, J.B. NASICON-type Li_{1+2x}Zr_{2-x}Ca_x(PO₄)₃ with high ionic conductivity at room temperature. *RSC Adv.* **2011**, *1*, 1728–1731. [[CrossRef](#)]
51. Liu, Y.; Li, C.; Li, B.; Song, H.; Cheng, Z.; Chen, M.; He, P.; Zhou, H. Germanium Thin Film Protected Lithium Aluminum Germanium Phosphate for Solid-State Li Batteries. *Adv. Energy Mater.* **2018**, *8*, 1702374. [[CrossRef](#)]



© 2020 by the authors. Licensee MDPI, Basel, Switzerland. This article is an open access article distributed under the terms and conditions of the Creative Commons Attribution (CC BY) license (<http://creativecommons.org/licenses/by/4.0/>).